

Low-temperature synthesis of tetragonal phase of hafnium oxide using polymer-blended nanofiber precursor

Ji-Won Jung^{a,1}, Ga-Yoon Kim^{b,1}, Na-Won Lee^b, Won-Hee Ryu^{b,c,*}

^a Department of Nuclear Science and Engineering, Massachusetts Institute of Technology, 77 Massachusetts Avenue, Cambridge, MA 02139, USA

^b Department of Chemical and Biological Engineering, Sookmyung Women's University, 100 Cheongpa-ro 47-gil, Yongsan-gu, Seoul 04310, Republic of Korea

^c Institute of Advanced Materials and Systems, Sookmyung Women's University, 100 Cheongpa-ro 47-gil, Yongsan-gu, Seoul 04310, Republic of Korea

ARTICLE INFO

Keywords:

Hafnium oxides
Nanofibers
Tetragonal phases
Low-temperature synthesis
Oxygen reduction and evolution reactions

ABSTRACT

Hafnium oxide (HfO_2), which is known as hafnia, is considered one of the best materials for various future applications such as neuromorphic computing systems and optical coatings. Although tetragonal phase (t-phase) in the multiple crystallographic structures of HfO_2 outperforms monoclinic phase (m-phase) most common phase that can be formed at low temperature in physicochemical properties such as dielectric constant, bandgap, high resistance to corrosion and hardness, it is extremely hard to stabilize t-phase below 1670 °C. Herein, we synthesized oxygen-deficient tetragonal hafnium oxide nanofibers (t- HfO_{2-x} NFs) using the electrospinning technique, which included the polymer-blended precursors and a magnesium-thermic reaction at a low processing temperature (< 600 °C). The small grain size (< 10 nm) of the t- HfO_{2-x} NFs and oxygen vacancies (V_{oxygen}) synergistically stabilized t-phase in the nanofibrous structure. Oxygen reduction reaction (ORR) and oxygen evolution reaction (OER) performances of the t- HfO_{2-x} NFs in alkaline and acid media were evaluated as a potential application, which were higher than those of the m- HfO_2 NFs. Our straightforward approach to make t-phase in HfO_2 -based materials can be broadly applied for many future applications.

1. Introduction

Diverse advanced technologies have motivated scientists and engineers to incorporate new, state-of-art materials into our modern lives. Hafnium oxide (HfO_2), also known as hafnia, has been employed as a versatile material in metal-oxide semiconductor devices, dynamic random access memory (DRAM) and optical coating owing to its high- k dielectric layer (~20 in monoclinic HfO_2 (m- HfO_2 , a monoclinic baddeleyite structure with space group $P2_1/c$)) with a large bandgap (5.7 eV) [1–4]. HfO_2 , a valve transition metal oxide family based on Group IV elements, has the same crystal structure as zirconium oxide (ZrO_2), but not as titanium oxide (TiO_2); m- HfO_2 is composed of metal center coordinated with seven or eight oxygen atoms [5]. The monoclinic phase can be transformed into a metastable tetragonal phase (t- HfO_2 , $P4_2/nmc$) by increasing the processing temperature to an extremely high value of ~1670 °C at atmospheric pressure, and it can be transformed into a cubic phase (c- HfO_2 , $Fm3m$) with further heating beyond ~2600 °C (Fig. 1(a)) [6,7]. These multiple crystallographic structures exhibit excellent physicochemical and mechanical properties, enabling them to be applied to a variety of applications [8,9]. The

production of m- HfO_2 at a low temperature is possible using simple methods such as sputtering and solution processing [10,11]. The t- and c- HfO_2 outperform the m- HfO_2 in parameters such as permittivity, bandgap, and catalytic activity, but the stabilization of the metastable t- HfO_2 and c- HfO_2 requires a very high temperature, which increases the complexity of the fabrication process [12,13].

Several researchers have attempted to reduce the processing temperature. The stabilization of the t- HfO_2 was often successful using deposition methods such as atomic layer deposition (ALD) and sputtering under low active oxygen source environment, pulse mode rapid annealing, and cation-doping method [8,14,15]. Another key approach that fascinated researchers was to stabilize the t- HfO_2 by reducing the grain size of HfO_2 to a nanometer scale [16]. This was achieved using methods such as thermal decomposition of pure $\text{Hf}(\text{OH})_4$, chemical reduction, sol-gel method, etc [17–19]. In these studies, the crystallite size of all t- HfO_2 was reduced to ~10 nm, which was a critical value in achieving the stabilization of the tetragonal structure [16]. Nevertheless, the processing methods developed so far are extremely complicated and time-consuming (> 2 days), which still remains a big challenge for stabilizing the tetragonal phase (t-phase) in HfO_2 .

* Corresponding author.

E-mail address: whryu@sookmyung.ac.kr (W.-H. Ryu).

¹ These authors contributed equally to this work.

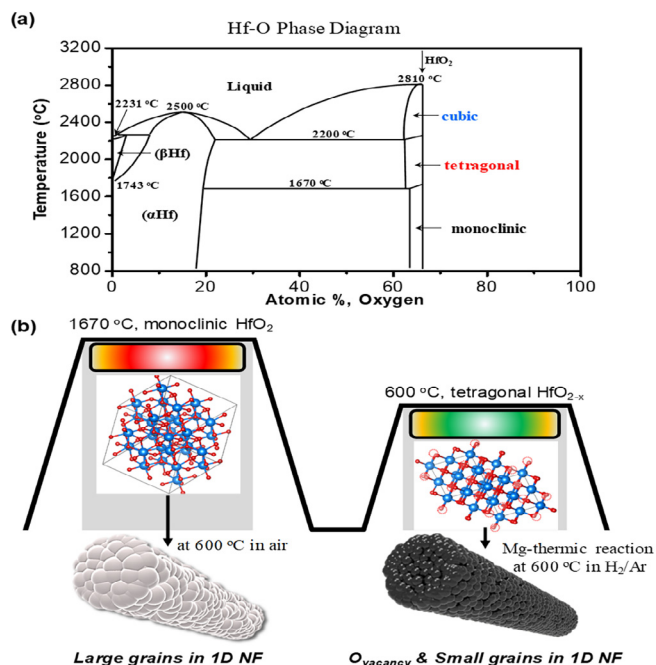


Fig. 1. (a) Temperature-composition phase diagram of Hf-O system. (b) Schematic illustration of a low processing temperature (< 600 °C) for synthesizing t-HfO_{2-x} with oxygen vacancies.

Herein, we suggested a new processing method to drive the formation of the novel t-phase of HfO_{2-x} at a low temperature. By combining electrospinning and magnesium-thermic reduction processes, a tetragonal phase-stabilized HfO_{2-x} nanofiber (t-HfO_{2-x} NF) with oxygen vacancies (V_{oxygen}) was achieved at a low temperature of 600 °C (Fig. 1(b)) [20]. With the assistance of Mg-thermic reduction reaction, the electrospun NFs were tuned as follows; (i) the distribution of homogeneous precursors in a one-dimensional (1D) nanofibrous matrix-induced small HfO_{2-x} crystallites (< 10 nm), and (ii) O₂ gas was liberated, which formed V_{oxygen} in the HfO_{2-x} NFs. The oxygen reduction reaction (ORR) and oxygen evolution reaction (OER) performances of the t-HfO₂ NFs were evaluated as a case study. The V_{oxygen} helped in stabilizing the t-phase at a low processing temperature, which remarkably enhanced the oxygen reduction activity due to an increase in the electronic conductivity and oxygen adsorption ability.

2. Materials and methods

2.1. Material synthesis

Monoclinic HfO₂ nanofibers (m-HfO₂ NFs) and tetragonal HfO_{2-x} NFs (t-HfO_{2-x} NFs) were synthesized using electrospinning and a subsequent two-step calcination process in different conditions. Electrospinning solution was prepared by dissolving Hf isopropoxide isopropanol adduct (C₁₂H₂₈HfO₄, 99.9%, Sigma-Aldrich) (2 g), dimethylformamide (DMF, 99.5%, Sigma-Aldrich) (10 g), acetic acid (99.7% (m/m), JUNSEI) (2 g), and polyvinylpyrrolidone (PVP, Mw ~1,300,000 by LS, Sigma-Aldrich) (1 g) and stirring the solution for 24 h. The solution was then loaded into a 12 mL syringe with a 25-gauge metal needle. The electrospinning process was executed at an applied voltage of 17 kV to obtain polymer-blended Hf NFs (PB-Hf NFs) as the precursor. The first calcination of the PB-Hf NFs was conducted at 350 °C for 1 h under air atmosphere, which was applied for both the m-HfO₂ NFs and t-HfO_{2-x} NFs in the same manner. Subsequently, the second calcination is carried out with the following different conditions: for the oxygen-deficient t-HfO_{2-x} NFs, a mixture of the pre-calcined NFs and magnesium powder (pre-calcined NFs:Mg = 1:1.5 (wt

%) was thermally treated under a Mg-reductive atmosphere (H₂ (5%)/Ar, v/v) at 600 °C for 4 h. Meanwhile, a post-thermal treatment under an air atmosphere at 600 °C for 4 h was conducted for forming the m-HfO₂ NFs. To remove the residual MgO impurities derived from the Mg-thermic reaction (HfO₂ + Mg → HfO_{2-x} + (MgO)_x), a concentrated hydrochloric acid (HCl, 1 N, SAMCHUN) solution was used; the MgO in the mixed powder (final product + MgO) was etched for one day, filtered, and washed with ethanol and distilled water several times. The etched samples were dried overnight under vacuum to achieve the t-HfO_{2-x} NFs as the final product.

2.2. Electrochemical characterization

Electrochemical measurements were carried out using three electrodes in a glass cell, which was composed of glassy carbon (working electrode with a diameter of 3 mm), Pt foil (counter electrode), and Ag/AgCl (NaCl, 3 M) reference electrode. The catalyst ink was prepared by ultrasonically scattering the solution containing 5 mg of catalyst, 50 μL of Nafion® perfluorinated resin solution and 500 μL of isopropyl alcohol (IPA, 99.9%, DAEJUNG). A 2 μL ink-loaded glassy carbon electrode (GCE) was employed on the rotating disk electrode (RDE) system at a specific potential. All the performance tests were carried out in O₂-saturated 0.1 M KOH and HClO₄ solutions. The measured potentials vs. Ag/AgCl were converted to the reversible hydrogen electrode (RHE) in accordance with the Nernst equation:

$$E_{\text{RHE}} = E_{\text{Ag/AgCl}} + 0.059 \text{ pH} + E^{\circ}_{\text{Ag/AgCl}}$$

where $E^{\circ}_{\text{Ag/AgCl}} = 0.1976$ at 25 °C and $E_{\text{Ag/AgCl}}$ is the experimentally recorded potential against Ag/AgCl reference. The oxygen reduction reaction (ORR) and oxygen evolution reaction (OER) curves were measured in the potential ranges of 0.1–1.1 V (vs. RHE) and 1.2–2.2 V (vs. RHE), respectively, with a scan rate of 5 mV/s at 1600 rpm using a potentiostat. The electron transfer number (*n*) was calculated utilizing Koutecky-Levich (K-L) equation.

Koutecky-Levich Equation: $j^{-1} = j_k^{-1} + j_d^{-1}$, where *j*, *j_k* and *j_d* are current density (A·cm⁻²), kinetic current density (A·cm⁻²) and diffusion-limited current density (A·cm⁻²).

j_d can be written: $0.62nFD_0^{2/3}\nu^{-1/6}C_0\omega^{1/2}$;

F is Faraday's Constant (96,485 C·mol⁻¹) and *D₀* is diffusion coefficient of O₂ in 0.1 M KOH (1.93×10^{-5} cm²·s⁻¹); *ν* is the kinematic viscosity of the electrolyte, 0.1 M KOH, (1.09×10^{-2} cm²·s⁻¹) and *C₀* is saturation concentration of O₂ in 0.1 M KOH at 1 atm O₂ pressure, (1.26×10^{-6} mol·cm⁻³); *ω*: rotation rate, rad·s⁻¹.

Here, $0.62FD_0^{2/3}\nu^{-1/6}C_0 = 1.152 \times 10^{-4}$ A·cm⁻²·s^{1/2}·rad^{-1/2}

2.3. Composition analysis

Composition analysis was carried out using X-ray photoelectron spectroscopy (XPS, K-alpha, Thermo VG Scientific). Both m-HfO₂ NFs and t-HfO_{2-x} NFs powders were loaded on a carbon tape (Okensoji) by 5 mm × 5 mm square. Subsequently, the carbon tapes were attached to a rigid substrate and moved to a chamber for measuring the binding energies using XPS. The binding energies were measured twice for each of the samples.

3. Results and discussion

We adopted electrospinning as a powerful technique that was capable of fabricating one-dimensional (1D) nanofibers (NFs) [21]. In this work, particularly, the electrospinning technique was used to precisely control the grain size of HfO₂ particles calcined from the polymer-blended Hf NF (PB-Hf NF) precursor; the crystallite size can be easily tuned by adjusting the calcination temperature for the PB-Hf NFs [22,23]. To investigate the thermal decomposition behaviors of the PB-Hf NFs, a thermogravimetric analysis (TGA) was conducted under an air atmosphere (Fig. 2(a)). A marginal weight loss at 100 °C is observed,

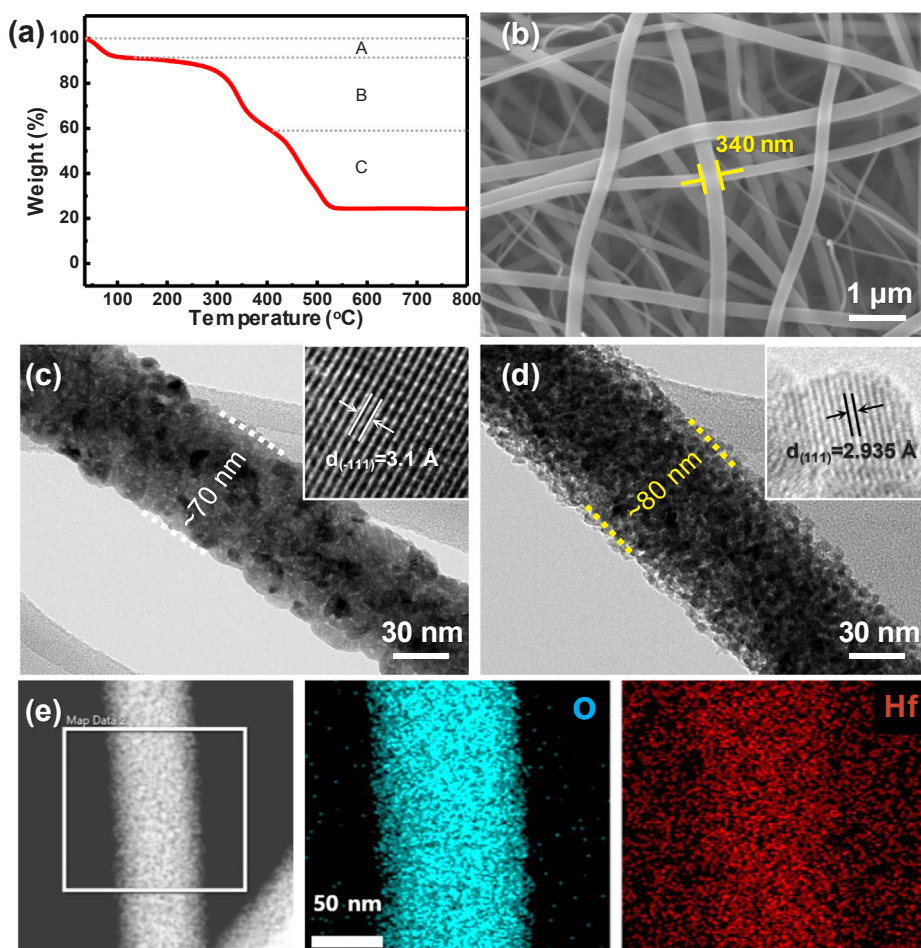


Fig. 2. (a) Thermogravimetric analysis (TGA) data of PB-Hf NFs in air. (b) SEM image of as-spun PB-Hf NFs. TEM images of (c) m-HfO₂ NFs and (d) t-HfO_{2-x} NFs. (e) STEM-EDS mapping image of t-HfO_{2-x} for elemental distribution of O (cyan) and Hf (red).

which is due to residual water in the PB-Hf NFs (region A). A second weight loss is then suddenly observed from approximately 300 to 525 °C (regions B and C) owing to the decomposition of polymer template (PVP) and chemical species in the precursor [20,24]. No further weight loss is observed beyond 525 °C under air atmosphere, implying that the oxidation of the m-HfO₂ NFs can be completed at 600 °C. Given that a perfect HfO₂ without defects is formed above 700 °C, the PB-Hf NFs can undergo much faster oxidation than other bulk materials studied in past literature [25]. As for the t-HfO_{2-x} NFs, we first treated the PB-Hf NFs thermally at a relatively low temperature of 350 °C. This was done not only to inhibit the growth of the HfO₂ crystallite but also to relax the crystal structure for conversion to HfO_{2-x} post the Mg-thermic reaction ($\text{HfO}_2 + \text{Mg} \rightarrow \text{HfO}_{2-x} + \text{MgO} + \Delta H$, where ΔH is the enthalpy generated during the reaction) at 600 °C under H₂/Ar (5%/95%, v/v) [26]. This two-step processing resulted in NFs having a tetragonal crystal structure with smaller grains (< 10 nm in size) and a higher number of V_{oxygen} (t-HfO_{2-x} NFs) as compared to that of the nondefective m-HfO₂ NFs achieved at 600 °C under air atmosphere. The morphological evolution of the PB-Hf NFs is confirmed using SEM (scanning electron microscope) and TEM (transmission electron microscopy) analyses, as shown in Fig. 2(b-d). It is observed that the relatively thick PB-Hf NFs have reduced in diameter (340 nm → ~70 nm and ~80 nm for the monoclinic HfO₂ NFs (m-HfO₂ NFs) and t-HfO_{2-x} NFs, respectively) after calcination. The m-HfO₂ NFs are composed of relatively large crystallites (> 10 nm) interconnected in a 1D structure (Fig. 2(c)). Meanwhile, small crystal particles (< 10 nm) were formed due to the Mg-thermic reaction, which might have been advantageous for the t-phase formation (Fig. 2(d)) [16]. The respective

insets show a highly magnified view corresponding to the (-111) plane with a lattice distance (= 3.1 Å) in the m-HfO₂ grain and (111) plane with d-spacing (= 2.935 Å) of the t-HfO_{2-x} grain [27]. This is supported by the high-resolution TEM (HR-TEM) images and selected area electron diffraction (SAED) patterns in Fig. S1, providing information on the different crystal sizes and different lattice planes in monoclinic and tetragonal phases. A scanning TEM energy-dispersive X-ray spectroscopy (STEM-EDS) was utilized to qualitatively map elements (Hf and O) distributed in the t-HfO_{2-x} NFs (Fig. 2(e)). Clearly, both Hf and O elements are well distributed in the 1D nanofibrous structure. The contents of residual carbon species in the m-HfO₂ NFs and t-HfO_{2-x} NFs after heat treatment were investigated by EDS analysis (Fig. S2). We analyzed three points EDS in the NFs and avg. contents of carbon in the m-HfO₂ NFs and t-HfO_{2-x} NFs are 1.23 and 2.98 wt%, respectively, both of which are negligible concerning the contribution of carbon to electronic conductivity and electrochemical performance.

To verify a particular crystalline phase of the m-HfO₂ NFs and t-HfO_{2-x} NFs, we carried out a powder X-ray diffraction (PXRD) analysis (Fig. 3(a)). The multiple peaks (pink lines) in the PXRD data correspond to the monoclinic structure of the HfO₂ in the m-HfO₂ NFs (JCPDS file no. 65-1142) [28]. It was confirmed that the crystalline nature of the non-stoichiometric t-HfO_{2-x} NFs was completely a tetragonal phase (JCPDS file no. 53-0550); the major peaks found at 30.38°, 35.20°, 50.68°, and 60.14° can be assigned to the (111), (200), (220) and (311) planes, respectively [27]. Raman spectroscopy was used to determine the vibrational modes in the HfO₂-based NFs (Fig. 3(b)). The Raman band at around 500 cm⁻¹ was a structural fingerprint of A_g mode in Hf-O of monoclinic HfO₂, which appeared in the m-HfO₂ NFs

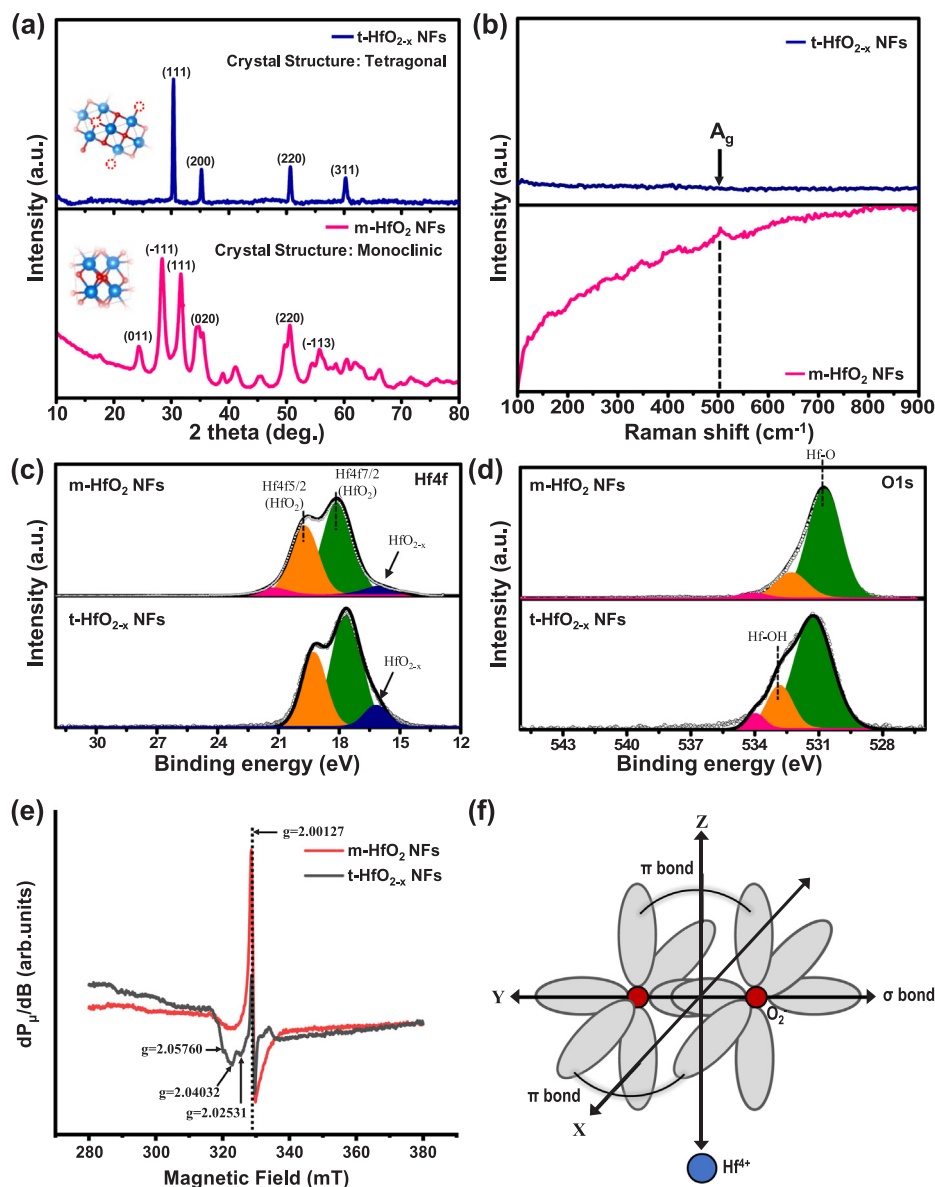


Fig. 3. (a) PXRD patterns and (b) Raman spectra of m-HfO₂ NFs and t-HfO_{2-x} NFs. Comparative XPS data of m-HfO₂ NFs and t-HfO_{2-x} NFs for (c) Hf 4f and (d) O 1s. (e) ESR data of both m-HfO₂ NFs and t-HfO_{2-x} NFs. (f) Schematic illustration of π wave functions for an O₂²⁻ defect in HfO₂.

[29]. In contrast, the band was absent in the t-HfO_{2-x} NFs, which constituted a critical feature of the tetragonal phase formed using our synthetic method. To gain insight into the V_{oxygen} for stabilizing the tetragonal phase, the X-ray photoelectron spectroscopy (XPS) was performed (Fig. 3(c) and 3(d)). For the m-HfO₂ NFs, the Hf 4f core-level spectra exhibited the doublet peaks located at 19.81 and 18.05 eV for Hf 4f5/2 and Hf 4f7/2 of HfO₂, respectively (Fig. 3(c)) [30]. These peaks shifted to lower binding energy in the t-HfO_{2-x} NFs, which is associated with the lower oxidation state (+4-2x) of Hf in the t-HfO_{2-x} NFs. More importantly, the intensity of the peak at 16.18 eV associated with the non-stoichiometric HfO_{2-x} in the t-HfO_{2-x} NFs was higher than that of the m-HfO₂ NFs. Moreover, for the core-level O 1s XPS peaks (Fig. 3(d)), the t-HfO_{2-x} NFs exhibited higher intensity of Hf-OH binding peak at ~532.81 eV, which suggested that t-HfO_{2-x} NFs had a large number of oxygen-deficient sites created due to the reductive calcination reaction; this indicated that the oxygen defects can bind with hydrogen atoms to form Hf-OH on the surface of the t-HfO_{2-x} NFs [31]. The peaks at around 534 eV can be assigned to C-O binding originated from the residual carbon species. For a closer investigation on the oxygen vacancy, electron spin resonance (ESR) was performed

for both m-HfO₂ NFs and t-HfO_{2-x} NFs (Fig. 3(e)). Generally, O₂²⁻ in HfO₂ has both σ and π bonding, as schematically shown in Fig. 3(f). Oxygen defects at different sites eliminate the degeneracy of the π bonding and antibonding levels on the basis of crystal field theory [32]. The 2p π_g orbitals are split up by this energy derived from the formation of the oxygen defect, relying on orbitals and bonding of free electrons. The free electrons at such defects can be detected by ESR, providing different values of g tensors ($g_{xx} = 2.00$, $g_{yy} = 2.01$, and $g_{zz} = 2.04$). In our case, the g-value of the m-HfO₂ NFs appeared at $g = 2.00127$, $g = 2.02531$, $g = 2.04032$, and $g = 2.05760$, which are well-matched with the g-values reported by Kanzig and Cohen [32]. Meanwhile, the t-HfO_{2-x} NFs showed a one sharp signal peak at $g = 2.00127$, which is for g_{xx} . This is indicative of a larger amount of oxygen vacancies in the t-HfO_{2-x} NFs compared with that of the m-HfO₂ NFs, which depends on the O₂²⁻ ions coordinated in different surroundings. From the above characteristics of the m-HfO₂ NFs and t-HfO_{2-x} NFs, we can infer that the V_{oxygen} might induce V_{Hf} (Schottky defect) or oxygen interstitial (Frenkel defect) as a charge-compensating element to satisfy charge neutrality. In general, the formation energy of the defects in the vicinity of metal sites was larger than that of the oxygen-relevant defects.

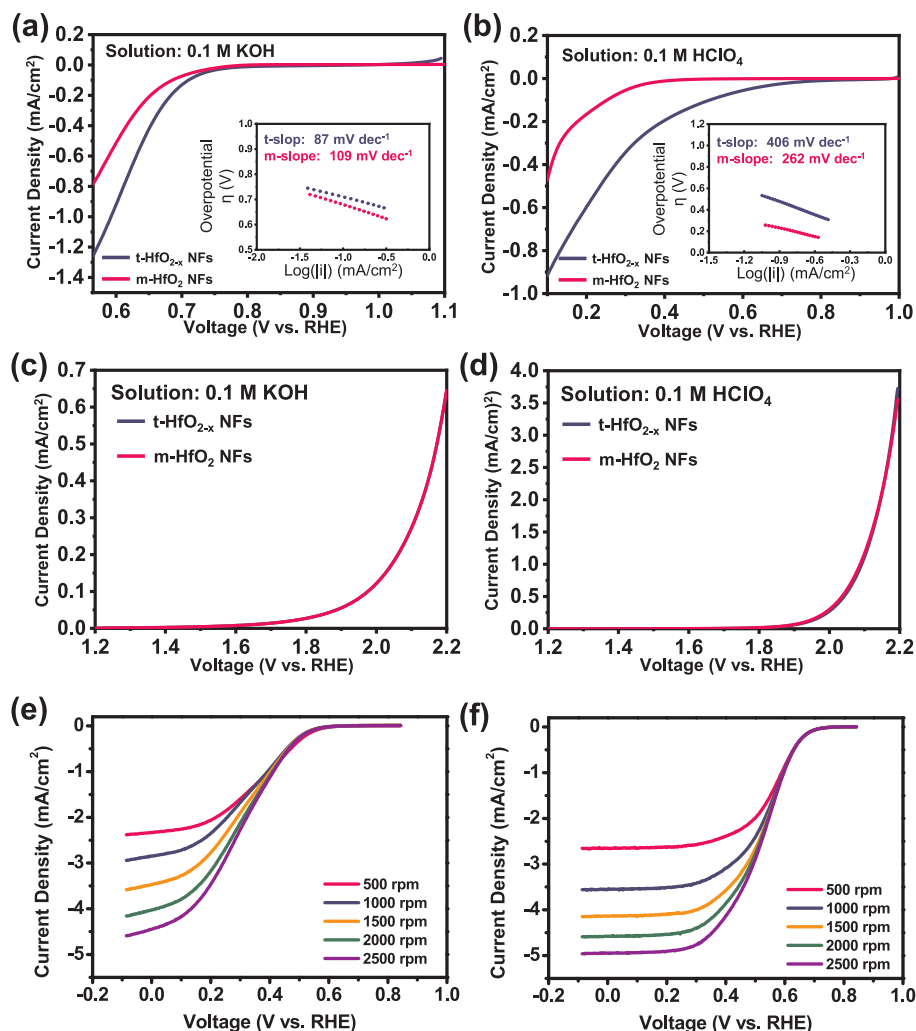


Fig. 4. (a,b) ORR and (c,d) OER polarization curves of m-HfO₂ NFs and t-HfO_{2-x} NFs in the O₂-saturated 0.1 M KOH and 0.1 M HClO₄ solutions, achieved using a rotating disk electrode with a rotating speed of 1600 rpm. ORR polarization curves of (e) m-HfO₂ NFs and (f) t-HfO_{2-x} NFs at various rotating speeds (500–2500 rpm) in 0.1 M KOH solution.

Therefore, V_{oxygen} can be considered as the primary source of the defect [33]. Schneider et al. assessed the influence of anion sublattice configuration on the energetics for several HfO_{2-x} phases [34]. They claimed that the V_{oxygen} promoted the noncentrosymmetric structure and energetically favored the t-phase, stabilizing the t-phase in the HfO_{2-x} crystal structure.

To identify the potential application of the low-temperature synthesized t-HfO_{2-x} NFs, the catalytic activities of oxygen reduction reaction (ORR) and oxygen evolution reaction (OER) were evaluated as a case study (Fig. 4). The electrochemical activities were investigated using the rotating disk electrode (RDE) measurements in 0.1 M KOH and HClO₄ solutions. Although the ORR current density (-0.8 to -1.3 mA cm⁻² in an alkaline solution) values are quite low, the t-HfO_{2-x} NFs outperformed the m-HfO₂ NFs considering the onset potentials; the t-HfO_{2-x} NFs have higher onset potential of 0.691 V as compared to that of the m-HfO₂ NFs (0.683 V) (Fig. 4(a)). The ORR onset potential of the t-HfO_{2-x} NFs (0.393 V) in an acid solution, which increased by 188 mV, was higher as compared to that of the m-HfO₂ NFs (0.205 V) (Fig. 4(b)). Moreover, the t-HfO_{2-x} NFs exhibited a moderate increase in the cathodic current densities, whereas the m-HfO₂ NFs exhibited a negligible increase in the ORR activity. The Tafel slope of the t-HfO_{2-x} NFs is 87 mV dec⁻¹ in an alkaline medium, which is a smaller value than that of the m-HfO₂ NFs (109 mV dec⁻¹); in an acid medium, the Tafel slope of the t-HfO_{2-x} NFs (406 mV dec⁻¹) is

larger than that of the m-HfO₂ NFs (262 mV dec⁻¹), which might be attributed to a different reaction path for the ORR (insets in Fig. 4(a) and 4(b), which is supported by the Tafel plots shown in Fig. S3). The good electrochemical performances of the t-HfO_{2-x} NFs are associated not only with the V_{oxygen} but also with a high electronic conductivity as a result of the reductive calcination using the Mg-thermic reaction. The V_{oxygen} , especially surface V_{oxygen} , is known as an active site for the adsorption of oxygen species [35]. The V_{oxygen} at the surface of the t-HfO_{2-x} NFs facilitates the adsorption of O₂, catalyzing the ORR in the KOH and HClO₄ media [36]. The presence of the V_{oxygen} can also modify Hf-O coordination in the tetragonal structure, which changes the defect states to generate a hole-conducting defect band at the Fermi level ($E_{\text{band}} < 5.7$ eV) [37]. The V_{oxygen} played critical roles in increasing the number of catalytic sites and electronic conductivity of the t-HfO_{2-x} NFs, thereby synergistically enhancing the ORR activity. To understand the enhanced electronic conductivity, we analyzed the reflectance rates and calculated the bandgaps of the both NFs based on Tauc equation (See details in Materials and Methods section, and Fig. S4) [38]. It is apparent that the m-HfO₂ NFs showed higher reflectance rates than those of the t-HfO_{2-x} NFs. The t-HfO_{2-x} NFs have much smaller bandgap (2.15 eV) compared with the m-HfO₂ NFs (4.4 eV), meaning that the t-HfO_{2-x} NFs have undoubtedly a higher electronic conductivity. We can rule out the effect of the residual carbon species on the improved electronic conductivity due to the negligible amount of

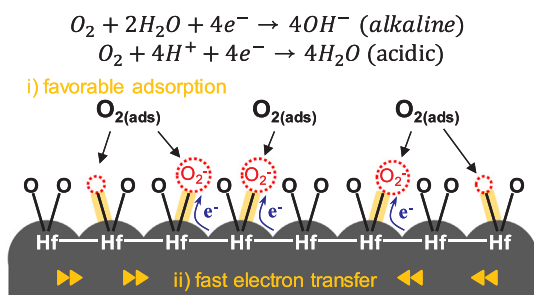


Fig. 5. Proposed ORR mechanism of t-HfO_{2-x} NFs.

the residues (~3 wt%). The OER current densities of the m-HfO₂ NFs and t-HfO_{2-x} NFs were monitored as a function of potential (Fig. 4(c) and 4(d)). However, the current values obtained in the alkaline and acid media are almost the same for both the samples, implying that the V_{oxygen} in the t-HfO_{2-x} NFs are not bifunctional catalytic sites for the ORR and OER; however, they are catalytic sites only for the ORR.

To propose the ORR mechanism of the m-HfO₂ NFs and t-HfO_{2-x} NFs, the RDE experiments were performed at various rotating speeds (500–2500 rpm) (Fig. 4(e,f)). The electron transfer number (*n*) for ORR was calculated using Koutecky-Levich (K-L) equation. The K-L plots of the m-HfO₂ NFs and t-HfO_{2-x} NFs are shown in Fig. S5, revealing a linear relationship between j^{-1} and $\omega^{-1/2}$, where *j* is current density (A·cm⁻²) and ω is rotation rate (rad·s⁻¹). The slopes of K-L plots of the m-HfO₂ NFs and t-HfO_{2-x} NFs are 2676.4 and 2229.1 cm² A⁻¹ S^{-1/2} rad^{1/2}, respectively. The *n* value of the t-HfO_{2-x} NFs is ~3.8, which is higher than that of the m-HfO₂ NFs (~3.25). This indicates much perfect selectivity of the t-HfO_{2-x} NFs for an active 4-electron ORR pathway. Moreover, the onset potential and current density of the t-HfO_{2-x} NFs are comparable to those of the commercial Pt/C electrode (Fig. S6). Based on the estimated *n* values, the V_{oxygen}-originated mechanism is schematically illustrated in Fig. 5. We think that what differentiates t-HfO_{2-x} NFs from the m-HfO₂ NFs is the anionic defect (V_{oxygen}). Generally, (i) the V_{oxygen} has lower adsorption energy than that of a perfect surface where atoms do not deviate from their regular coordination numbers. This makes it attractive to O₂ in an aqueous electrolyte; this facilitates an overall ORR based on representative 4-electron pathways in the alkaline (O₂ + 2H₂O + 4e⁻ → 4OH⁻) and acid media (O₂ + 4H⁺ + 4e⁻ → 4H₂O) [39]. (ii) The V_{oxygen} sites in the t-HfO_{2-x} NFs adsorb O₂, and the O₂ cleavage/charge transfer can be promoted due to the enhanced electronic conductivity; the defects create shallow energy states between the conduction and valence band, increasing the entire electronic conductivity (e.g., reduced bandgap or p-type semiconducting property). Considering all the observations, we expect that the key for catalyzing the ORR in the HfO₂ NFs is to create V_{oxygen} at the surface and in bulk (the effect of phases in HfO₂ on the ORR performance has not been presented here).

4. Conclusion

In conclusion, we have tapped into the electrospinning technique using the polymer-blended precursors (PBP) and reductive Mg-thermic calcination to successfully synthesize the tetragonal hafnium oxide with oxygen vacancies (t-HfO_{2-x} NFs) at a low-temperature (< 600 °C). The oxygen vacancies (V_{oxygen}) were induced in the t-HfO_{2-x} NFs, which stabilized the metastable t-phase in the 1D HfO_{2-x} NFs. The engineering of the anionic defects (V_{oxygen}) provided a large number of active sites and an enhanced electronic conductivity. As a result, the electrochemical catalytic activity of the oxygen reduction reaction (ORR) for the t-HfO_{2-x} NFs was highly improved as compared to that for the m-HfO₂ NFs. This synthetic method could be applied to various applications.

CRediT authorship contribution statement

Ji-Won Jung: Writing - original draft, Conceptualization, Investigation, Data curation, Formal analysis, Visualization. **Ga-Yoon Kim:** Writing - review & editing, Conceptualization, Investigation, Data curation, Formal analysis, Visualization. **Na-Won Lee:** Methodology, Investigation, Data curation. **Won-Hee Ryu:** Conceptualization, Methodology, Supervision, Writing - review & editing, Project administration, Funding acquisition.

Declaration of Competing Interest

The authors declare that they have no known competing financial interests or personal relationships that could have appeared to influence the work reported in this paper.

Acknowledgment

This work was supported by the National Research Foundation of Korea (NRF) grant funded by the Korean government (MSIT) (No. 2019R1C1C1007886, 2019M3D1A2104105 and 2018R1A5A1025224).

Appendix A. Supplementary material

Supplementary data to this article can be found online at <https://doi.org/10.1016/j.apsusc.2020.147496>.

References

- [1] G.D. Wilk, R.M. Wallace, J.M. Anthony, High-k gate dielectrics: current status and materials properties considerations, *J. Appl. Phys.* 89 (2001) 5243–5275.
- [2] M.C. Cheynet, S. Pokrant, F.D. Tichelaar, J.L. Rouvire, Crystal structure and band gap determination of HfO₂ thin films, *J. Appl. Phys.* 101 (2007) 054101.
- [3] E. Bersch, S. Rangan, R.A. Bartynski, E. Garfunkel, E. Vescovo, Band offsets of ultrathin high-k oxide films with Si, *Phys. Rev. B* 78 (2008) 085114.
- [4] J.H. Choi, Y. Mao, J.P. Chang, Development of hafnium based high-k materials - A review, *Mater. Sci. Eng. R Reports* 72 (2011) 97–136.
- [5] T.V. Perevalov, V.A. Gritsenko, S.B. Erenburg, A.M. Badalyan, H. Wong, C.W. Kim, Atomic and electronic structure of amorphous and crystalline hafnium oxide: X-ray photoelectron spectroscopy and density functional calculations, *J. Appl. Phys.* 101 (2007) 053704.
- [6] T.B. Massalski, *Binary Alloy Phase Diagrams*, ASM International, Materials Park, Ohio, 1990.
- [7] O. Ohtaka, H. Fukui, T. Kunisada, T. Fujisawa, K. Funakoshi, W. Utsumi, T. Irifune, K. Kuroda, T. Kikegawa, Phase relations and volume changes of hafnia under high pressure and high temperature, *J. Am. Ceram. Soc.* 84 (2004) 1369–1373.
- [8] B. Cojocaru, D. Avram, R. Negrea, C. Ghica, V.G. Kessler, G.A. Seisenbaeva, V.I. Parvulescu, C. Tiseanu, Phase control in hafnia: new synthesis approach and convergence of average and local structure properties, *ACS Omega* 4 (2019) 8881–8891.
- [9] M. Raza, S. Sanna, L. Dos Santos Gómez, E. Gautron, A.A. El Mel, N. Pryds, R. Snyders, S. Konstantinidis, V. Esposito, Near interface ionic transport in oxygen vacancy stabilized cubic zirconium oxide thin films, *Phys. Chem. Chem. Phys.* 20 (2018) 26068–26071.
- [10] N.W. Pi, M. Zhang, J. Jiang, A. Belosludtsev, J. Vlček, J. Houška, E.I. Meletis, Microstructure of hard and optically transparent HfO₂ films prepared by high-power impulse magnetron sputtering with a pulsed oxygen flow control, *Thin Solid Films* 619 (2016) 239–249.
- [11] P. Blanc, A. Larbot, J. Palmeri, M. Lopez, L. Cot, Hafnia ceramic nanofiltration membranes. Part I: Preparation and characterization, *J. Memb. Sci.* 149 (1998) 151–161.
- [12] I. Salem, Recent studies on the catalytic activity of titanium, zirconium, and hafnium oxides, *Catal. Rev. Sci. Eng.* 45 (2003) 205–296.
- [13] T. Tobase, A. Yoshiasa, H. Arima, K. Sugiyama, O. Ohtaka, T. Nakatani, K. Ichi Funakoshi, S. Kohara, Pre-transitional behavior in tetragonal to cubic phase transition in HfO₂ revealed by high temperature diffraction experiments, *Phys. Status Solidi B* 255 (2018) 1800090.
- [14] D.Y. Cho, H.S. Jung, I.H. Yu, J.H. Yoon, H.K. Kim, S.Y. Lee, S.H. Jeon, S. Han, J.H. Kim, T.J. Park, B.G. Park, C.S. Hwang, Stabilization of tetragonal HfO₂ under low active oxygen source environment in atomic layer deposition, *Chem. Mater.* 24 (2012) 3534–3543.
- [15] C.W. Lin, Y.T. Chiang, Tetragonal hafnium oxide film prepared by low-temperature oxidation, *Jpn. J. Appl. Phys.* 53 (2014) 11RA07.
- [16] O. Hunter, R.W. Scheidecker, S. Tojo, Characterization of metastable tetragonal hafnia, *Ceramurg. Int.* 5 (1979) 137–142.
- [17] G.R. Waetzig, S.W. Depner, H. Asayesh-Ardakani, N.D. Cultrara, R. Shahbazian-

- Yassar, S. Banerjee, Stabilizing metastable tetragonal HfO_2 using a non-hydrolytic solution-phase route: Ligand exchange as a means of controlling particle size, *Chem. Sci.* 7 (2016) 4930–4939.
- [18] B. Matovic, J. Pantic, J. Lukovic, M. Cebela, S. Dmitrovic, M. Mirkovic, M. Prekajski, A novel reduction–oxidation synthetic route for hafnia, *Ceram. Int.* 42 (2016) 615–620.
- [19] J. Tang, J. Fabbri, R.D. Robinson, Y. Zhu, I.P. Herman, M.L. Steigerwald, L.E. Brus, Solid-solution nanoparticles: use of a nonhydrolytic sol-gel synthesis to prepare HfO_2 and $\text{Hf}_x\text{Zr}_{1-x}\text{O}_2$ nanocrystals, *Chem. Mater.* 16 (2004) 1336–1342.
- [20] N.W. Lee, K.R. Yoon, J.Y. Lee, Y. Park, S.J. Pyo, G.Y. Kim, D.H. Ha, W.H. Ryu, Highly conductive off-stoichiometric zirconium oxide nanofibers with controllable crystalline structures and bandgaps and improved electrochemical activities, *ACS Appl. Energy Mater.* 2 (2019) 3513–3522.
- [21] J.W. Jung, C.L. Lee, S. Yu, I.D. Kim, Electrospun nanofibers as a platform for advanced secondary batteries: A comprehensive review, *J. Mater. Chem. A* 4 (2016) 703–750.
- [22] A.S. Nair, Y. Shengyuan, Z. Peining, S. Ramakrishna, Rice grain-shaped TiO_2 mesostructures by electrospinning for dye-sensitized solar cells, *Chem. Commun.* 46 (2010) 7421–7423.
- [23] J.W. Jung, W.H. Ryu, S. Yu, C. Kim, S.H. Cho, I.D. Kim, Dimensional effects of MoS_2 nanoplates embedded in carbon nanofibers for bifunctional Li and Na insertion and conversion reactions, *ACS Appl. Mater. Interfaces* 8 (2016) 26758–26768.
- [24] S.H. Choi, I.S. Hwang, J.H. Lee, S.G. Oh, I.D. Kim, Microstructural control and selective $\text{C}_2\text{H}_5\text{OH}$ sensing properties of Zn_2SnO_4 nanofibers prepared by electrospinning, *Chem. Commun.* 47 (2011) 9315–9317.
- [25] H. Wong, K.L. Ng, N. Zhan, M.C. Poon, C.W. Kok, Interface bonding structure of hafnium oxide prepared by direct sputtering of hafnium in oxygen, *J. Vac. Sci. Technol. B Microelectron. Nanom. Struct.* 22 (2004) 1094–1100.
- [26] M. Aeronautical, M. Engineering, Review of thermite reactions, *J. Mater. Sci.* 28 (1993) 3693–3708.
- [27] Y. Wan, X. Zhou, Formation mechanism of hafnium oxide nanoparticles by a hydrothermal route, *RSC Adv.* 7 (2017) 7763–7773.
- [28] S. Yun, H. Zhou, L. Wang, H. Zhang, T. Ma, Economical hafnium oxygen nitride binary/ternary nanocomposite counter electrode catalysts for high-efficiency dye-sensitized solar cells, *J. Mater. Chem. A* 1 (2013) 1341–1348.
- [29] D.S. Kumar, K. Ananthasivan, R. Venkata Krishnan, S. Amirthapandian, T.R. Ravindran, S. Balakrishnan, Synthesis of monoclinic and cubic (metastable) nanocrystalline HfO_2 through the nitrate fusion technique, *Ceram. Int.* 43 (2017) 12623–12632.
- [30] S.U. Sharath, T. Bertaud, J. Kurian, E. Hildebrandt, C. Walczyk, P. Calka, P. Zaumseil, M. Sowinska, D. Walczyk, A. Gloskovskii, T. Schroeder, L. Alff, Towards forming-free resistive switching in oxygen engineered HfO_{2-x} , *Appl. Phys. Lett.* 104 (2014) 063502.
- [31] A.A. Rastorguev, V.I. Belyi, T.P. Smirnova, L.V. Yakovkina, M.V. Zamoryanskaya, V.A. Gritsenko, H. Wong, Luminescence of intrinsic and extrinsic defects in hafnium oxide films, *Phys. Rev. B* 76 (2007) 235315.
- [32] A.Y. Kang, P.M. Lenahan, Electron spin resonance observation of trapped electron centers in atomic-layer-deposited hafnium oxide on Si, *Appl. Phys. Lett.* 83 (2003) 3407–3409.
- [33] J.X. Zheng, G. Ceder, T. Maxisch, W.K. Chim, W.K. Choi, First-principles study of native point defects in hafnia and zirconia, *Phys. Rev. B* 75 (2007) 104112.
- [34] K. Sarakinos, D. Music, S. Mráz, M. To Baben, K. Jiang, F. Nahif, A. Braun, C. Zilkens, S. Konstantinidis, F. Renaux, D. Cossement, F. Munnik, J.M. Schneider, On the phase formation of sputtered hafnium oxide and oxynitride films, *J. Appl. Phys.* 108 (2010) 014904.
- [35] Q. Kang-Wen, C. Xi, Y. Zhang, R. Zhang, Z. Li, G.R. Sheng, H. Liu, C.K. Dong, Y.J. Chen, X.W. Du, Laser-induced oxygen vacancies in FeCo_2O_4 nanoparticles for boosting oxygen evolution and reduction, *Chem. Commun.* 55 (2019) 8579–8582.
- [36] J. Greeley, N.M. Markovic, The road from animal electricity to green energy: Combining experiment and theory in electrocatalysis, *Energy Environ. Sci.* 5 (2012) 9246–9256.
- [37] E. Hildebrandt, J. Kurian, M.M. Miller, T. Schroeder, H.J. Kleebe, L. Alff, Controlled oxygen vacancy induced p-type conductivity in HfO_{2-x} thin films, *Appl. Phys. Lett.* 99 (2011) 112902.
- [38] V.M. Huxter, T. Mirkovic, P.S. Nair, G.D. Scholes, Demonstration of bulk semiconductor optical properties in processable Ag_2S and EuS nanocrystalline systems, *Adv. Mater.* 20 (2008) 2439–2443.
- [39] Y. Zhu, X. Liu, S. Jin, H. Chen, W. Lee, M. Liu, Y. Chen, Anionic defect engineering of transition metal oxides for oxygen reduction and evolution reactions, *J. Mater. Chem. A* 7 (2019) 5875–5897.